

Bio-inspired NiCoP/CoMoP/Co(Mo₃Se₄)₄ @C/NF multi-heterojunction nanoflowers : Effective catalytic nitrogen reduction by driving electron transfer

Xin Li ^{a,b}, Guangtong Hai ^a, Jin Liu ^c, Fenglin Zhao ^a, Zehua Peng ^b, Honghong Liu ^d, Michael K. H. Leung ^{b,*}, Haihui Wang ^{a,*}

^a Department of Chemical Engineering, Tsinghua University, Beijing 100084, China

^b Ability R&D Energy Research Centre, School of Energy and Environment, City University of Hong Kong, Kowloon 999077, Hong Kong Special Administrative Region of China

^c Yellow River Institute of Eco-Environment Research, Zhengzhou 450100, China

^d Laboratory of Enhanced Heat Transfer and Energy Conservation, The Ministry of Education, School of Chemistry and Chemical Engineering, South China University of Technology, Guangzhou 510640, China



ARTICLE INFO

Keywords:

Nitrogen reduction reaction
Electron redistribution
Multiple heterojunction interfaces
Biomimetic electrocatalyst

ABSTRACT

Electrochemical nitrogen reduction reaction can be adopted to generate renewable ammonia. That is recognized as a sustainable alternative to the Haber-Bosch process. However, the limited electrocatalytic activity remains the primary obstacle against viable application of the electrocatalytic ammonia fixation. Herein, a biomimetic three-dimensional NiCoP/CoMoP/Co(Mo₃Se₄)₄ @C/NF electrocatalyst is designed to have excellent NRR performance with an NH₃ yield rate of 24.54 μg h⁻¹ cm⁻² and Faradaic efficiency of 23.15%. Based on the experimental and theoretical results, NiCoP/CoMoP/Co(Mo₃Se₄)₄ @C/NF electrocatalyst perfectly simulates the structural characteristics of biological nitrogenase, where Co(Mo₃Se₄)₄ acts as the major active center while NiCoP and CoMoP contribute to controlling the electron transfer during NRR. Additionally, the coexistence of the three different heterojunction interfaces induces more effective electronic structure modulation compared with the single interface, thereby optimizing the reaction energy barrier of intermediates. This work has developed a synergistic strategy to boost the reaction kinetics via introducing multiple heterojunction interfaces.

1. Introduction

Ammonia (NH₃) is essential to sustain human life and global economic development as a commodity material, fertilizer feedstock, chemical precursor and newly identified as an effective hydrogen storage medium and carbon-free emission fuel [1]. However, the current industrial method for ammonia production is still heavily dependent upon the traditional Haber-Bosch process (HBP), which is extremely energy- and capital-intensive [2]. Electrochemical nitrogen reduction reaction (NRR) has recently been considered as the most promising alternative to substitute for the Haber-Bosch process due to its mild operation conditions at the ambient temperature and normal atmospheric pressure [3–8], which involves the potential coupling with green energy for the reaction without CO₂ emission and the utilization of abundant water instead of high purity hydrogen gas [9–12].

Unfortunately, the practical application is still challenging mainly because the strong dinitrogen bond is difficult to cleave and the competitive hydrogen reduction reaction (HER) occurs simultaneously, resulting in low NH₃ yield rate and NRR efficiency [13,14].

In the natural world, only certain nitrogenase bacteria can selectively break the non-polar N≡N triple bonds to realize the conversion of nitrogen to ammonia [15]. This enzyme complex nitrogenase is composed of three essential metalloproteins: (1) MoFe₇S₉C cofactor functions as the key active site to catalytic reduction of nitrogen; (2) Fe₄S₄ is used to facilitate hydrolysis of MgATP and electron transfer to the MoFe₇S₉C and (3) Fe₈S₇ is responsible for transferring electrons to the MoFe₇S₉C from the Fe₄S₄ cluster [16]. Based on the above mechanism analysis, researchers realize that it is difficult to achieve excellent NRR performance with a single composition catalyst. Therefore, several compounds containing transition metallic Fe, Co and Mo [17–22], and

* Corresponding authors.

E-mail addresses: mkh.leung@cityu.edu.hk (M.K.H. Leung), cehhwang@tsinghua.edu.cn (H. Wang).

nonmetallic O, Se, N, P, and S, have been extensively investigated to mimic the nitrogenase structure and previous studies have achieved considerable progress for the fixation of nitrogen to ammonia [23–26]. However, the efficiency obtained is still far from satisfactory for practical applications [27–31]. For instance, Guo et al. reported that the rational arrangement of bio-inspired FeMoS catalysts could generate NH₃ at a yield rate of 8.75 µg h⁻¹ cm⁻² at –0.5 V, while the Faradaic efficiency is only 2.96% [32]. The main reason is that the bond strength between nitrogen and metal is too weak for N₂ activation and the d-orbital electrons in transition metals favor the formation of metal–H bond for adverse HER, both of which would give rise to a compromising Faradaic efficiency [33–37]. Therefore, transformative advances in electrocatalytic NRR may be expected from exploiting appropriate strategies to modify the interfacial properties of materials and to optimize the adsorption behavior of intermediates.

Theoretically, the ideal NRR electrocatalysts should have appropriate adsorption energy for intermediates on materials surface, that is neither too strong nor too weak [38,39]. Moreover, the adsorption energies of nitrogen should be lower than that of hydrogen, thereby enhancing the NRR selectivity and suppressing the competing HER. To this end, interface engineering could be a viable route for the following reasons. Firstly, owing to the mismatched lattice at the interface between different components, the heterostructures involving disorder, defects, and multiple phases could expose more catalytically active sites [40–44]. Secondly, strong interfacial interactions also contribute to the establishment of more channels for the charge and mass transfer [45,46], inducing better electronic coupling effect and optimizing the free energies of intermediates [47,48]. Last but not the least, the robust contact interfaces between different components directly provide superior electronic conductivity and excellent mechanical stability [49]. Therefore, by regulating the electron density of the heterostructure interface, the adsorption and desorption of intermediate products can be further optimized. Enlightened by these advantages, it is logical to anticipate that outstanding NRR performance can be achieved by introducing interface engineering into bio-inspired electrocatalysts, which still lacks exploration.

Herein, for the first time, a novel bio-inspired electrocatalyst of three-dimensional (3D) NiCoP/CoMoP/Co(Mo₃Se₄)₄ @C/NF is rationally designed to perfectly simulate the structural characteristics of biological nitrogenase. Surprisingly, triple heterojunction interfaces are simultaneously formed, (i.e., NiCoP-CoMoP, NiCoP-Co(Mo₃Se₄)₄ and NiCoP-Co(Mo₃Se₄)₄) during the synthesis of the electrocatalyst. They coordinate to extend the catalytically active sites and optimize the reaction energy barrier of the intermediates. Our density functional theory (DFT) calculations reveal that CoMoP can be used as an electron carrier to transfer electrons from NiCoP to Co(Mo₃Se₄)₄. As a result, a lot of electrons are accumulated in Co(Mo₃Se₄)₄ and significantly decrease the energy barrier for the first hydrogenation of NRR. Additionally, the electron redistribution induced by the triple heterostructure electron coupling leads to a high electrical conductivity and contributes to a high interconnectivity to enable elevated charge transfer for an efficient electrocatalytic reaction, which effectively optimizes the adsorption behavior of intermediates. As expected, the 3D-networked NiCoP/CoMoP/Co(Mo₃Se₄)₄ @C/NF multi-heterojunction nanoflowers exhibit outstanding NRR performance in 0.1 M Na₂SO₄ solution with an NH₃ yield rate of 24.54 µg h⁻¹ cm⁻² and Faradaic efficiency of 23.15% (measured in a gas-tight H-type cell with a three-electrode configuration under ambient conditions), which are severalfold superior to most of the previously reported compounds based on non-precious metal. The NiCoP/CoMoP/Co(Mo₃Se₄)₄ @C/NF also demonstrates long-term stability up to 24 h of N₂ reduction reaction without noticeable performance degradation. In this work, the highly conductivity of the carbon shell, strong interfacial coupling effects between triple heterojunctions, and the unique 3D hierarchical architecture that mimics the biological nitrogenase are the main factors that contribute to the improved NRR performance and suppressed HER activity.

2. Experimental

2.1. Chemicals and materials

All chemicals and solvents were consumed without any further modification, including sodium molybdate dihydrate (Na₂MoO₄·2 H₂O, 99%, J&K scientific), cobalt nitrate hexahydrate (Co(NO₃)₂·6H₂O, 98.0 + %, Sigma-Aldrich), urea (CO(NH₂)₂, 99.0%, Sigma-Aldrich), ammonium fluoride (NH₄F, 99.0%, Sigma-Aldrich), selenium powder (Se, 99.5%, J&K scientific), sodium hypophosphite (NaH₂PO₂·xH₂O, 99.0%, Sigma-Aldrich), and sodium sulfate (Na₂SO₄, 99.0%, Sigma-Aldrich). A nickel foam with 110 pores per inch (PPI) and 1 mm thickness was used in the experiment.

2.2. Catalyst preparation

2.2.1. Pretreatment of nickel foam

Firstly, nickel foams of size 1 × 5 cm² were cut and then pretreated with concentrated HCl solution in a sonication dispenser for 20 min to remove the impurities and oxidation layers. Then, the nickel foam pieces were alternately ultrasonic cleaned with ethanol and distilled water for 3 times, followed by vacuum drying at 40 °C.

2.2.2. Synthesis of NiCoP/CoMoP/Co(Mo₃Se₄)₄ @C/NF

In a normal procedure, 3 mM of Co(NO₃)₂·6 H₂O, 2 mM of Na₂MoO₄·2H₂O, 2 mM of urea and 2 mM of NH₄F were fully dispersed in 50 mL of deionized water and vigorously stirred for 4 h. Then, the mixture solution and Ni foams were transferred into a 100 mL Teflon-lined stainless-steel autoclave and heated at 120 °C for 5 h. After that, the obtained precipitates were washed step by step with ethanol and water for four times and vacuum dried overnight at 40 °C. Finally, 2 mM NaH₂PO₂·xH₂O, 2 mM Se powder and as prepared products were sequentially placed in the upstream, midstream and downstream of the tubular furnace, and then heated from room temperature to 350 °C for 1 h with a heating rate of 5 °C min⁻¹ under flowing nitrogen gas, followed by rising to 450 °C (5 °C min⁻¹) for another 1 h, leading to NiCoP/CoMoP/Co(Mo₃Se₄)₄ @C/NF.

2.2.3. Synthesis NiCoP/NF

3 mM of Co(NO₃)₂·6 H₂O, 3 mM of Ni(NO₃)₂, 2 mM of urea and 2 mM of NH₄F were fully dispersed in 50 mL of deionized water and vigorously stirred for 4 h. Then, the mixture solution and Ni foam were transferred into a 100 mL Teflon-lined stainless-steel autoclave and heated at 120 °C for 5 h. After that, the obtained precipitates were washed with ethanol and water in sequence for four times and vacuum dried overnight at 40 °C. Finally, 2 mM NaH₂PO₂·xH₂O and as prepared products were sequentially placed in the tubular furnace, and then heated from room temperature to 350 °C for 2 h, leading to NiCoP.

2.2.4. Synthesis of Co(Mo₃Se₄)₄ and CoMoP

3 mM of Co(NO₃)₂·6H₂O, 2 mM of Na₂MoO₄·2H₂O, 2 mM of urea and 2 mM of NH₄F were fully dispersed in 50 mL of deionized water and vigorously stirred for 4 h. Then, the mixture solution was transferred into a 100 mL Teflon-lined stainless-steel autoclave and heated at 120 °C for 5 h. After that, the obtained precipitates were washed with ethanol through centrifugation at 8000 rpm for 10 min for three times and vacuum dried overnight at 40 °C. Finally, 2 mM NaH₂PO₂·xH₂O and as prepared products were sequentially placed in the tubular furnace, and then heated from room temperature to 350 °C for 2 h, leading to CoMoP. Similarly, for the Co(Mo₃Se₄)₄, 2 mM Se powder and as prepared products were sequentially placed in the tubular furnace, and then heated from room temperature to 450 °C for 2 h.

2.3. Physicochemical characterization

The X-ray diffraction (XRD) patterns were recorded by a PANalytical

X'Pert3 power X-ray diffractometer at a scan rate of $20^\circ \cdot \text{min}^{-1}$ from 5° to 85° . The morphologies and microstructures of the prepared catalysts were characterized by a field-emission scanning electron microscope (SEM) instrument (ULTRA Plus), and a high-resolution transmission electron microscope (HRTEM, Talos F200X). Furthermore, the atomic-resolution high-angle annular dark-field transmission electron microscope (HAADF-STEM) images, energy-dispersive X-ray spectroscope (EDS) mappings were acquired by using an aberration-corrected scanning transmission electron microscope (AC-STEM) operating at 200 kV (JEOL 2200FS). The X-ray photoelectron spectroscopy (XPS) experiments were performed on an X-ray photoelectron spectrometer (Omicron, UHV Multiprobe XP, SPM) using Al-K α as the exciting source.

2.4. Electrochemical tests

All the electrochemical measurements were performed at room temperature using an electrochemical workstation (Gamry) with an H-type cell separated by a Nafion 211 membrane (pretreated by boiling in 5% H_2O_2 and deionized water at 80°C for 1 h respectively, followed by boiling in 0.5 M H_2SO_4 and finally washed with deionized water for four times). A standard three-electrode system was used to measure the electrochemical performance, in which synthesized catalysts, Ag/AgCl/ sat. KCl and According to the Nernst equation: $E_{\text{RHE}} = E_{\text{Ag}/\text{AgCl}} + E_{\text{Ag}/\text{AgCl}} + 0.059 \text{ PH}$, all the applied potentials in this work were measured against the Ag/AgCl/ sat. KCl and converted to the reversible electrode (RHE). The electrochemical NRR experiments were conducted in N_2 -saturated 0.1 M Na_2SO_4 with each compartment containing 60 mL of electrolyte (each electrolyte was purged with N_2 for at least 30 min to ensure the removal of residual air before each measurement). Linear sweep voltammetry (LSV) was scanned in the voltage window between -0.7 and 0 V vs. RHE at a rate of 5 mV s^{-1} , and the chronoamperometry tests were operated at different applied potentials ($-0.10, -0.15, -0.20, -0.25, -0.30, -0.35 \text{ V}$ vs. RHE) for 2 h. During the whole electrolysis process, the electrolyte was continuously bubbled with high purity N_2 (99.999%) with a flow rate of 20 sccm, and was agitated with a stirring bar at a stirring rate of about 800 rpm.

2.5. Products detection

2.5.1. Quantification of NH_3 with indophenol blue method

The quantity of NH_3 produced was measured by colorimetry using the indophenol blue method [50]. In details, 2 mL of the electrolyte after N_2 reduction reaction was mixed with 2 mL of the solution A (1 M NaOH solution containing 5 wt% sodium citrate and 5 wt% salicylic acid), 1 mL of the solution B (0.05 M sodium hypochlorite) and 0.2 mL of the solution C (1 wt% sodium nitroferricyanide). All test solutions were incubated under darkness for 2 h before Ultraviolet-visible (UV-vis) tests. The absorption spectra between 550 and 800 nm for above mixture were measured by a UV-vis spectrophotometer, and the formed indophenol blue was determined by absorbance at a wavelength of 655 nm. A series of reference solutions with suitable ammonium chloride (NH_4Cl) concentrations in 0.1 M Na_2SO_4 and 1 mM H_2SO_4 were used to plot standard concentration-absorbance curves. The background solution was used for measurements in all experiments, and the background peak was subtracted from the measured peaks of the N_2 reduction experiments to calculate the ammonia concentration and Faradaic efficiency.

2.5.2. Isotopic labeling experiment

An isotopic labeling experiment used $^{15}\text{N}_2$ (98 atom%, Sigma-Aldrich) as the gas reactant was performed to clarify the source of ammonia. After 5 h $^{15}\text{N}_2$ reduction reaction at -0.2 V (vs. RHE) in a 0.1 M Na_2SO_4 , the electrolyte was acidized to pH 1 by 1 M HCl and then concentrated to 1 mL via distillation at 90°C . Finally, the obtained $^{15}\text{NH}_4^+$ was measured using ^1H NMR (400 Hz) spectroscopy.

2.5.3. Quantification of byproducts N_2H_4 with Watt-Chrisp method

The probable byproduct of hydrazine was measured by the Watt-Chrisp method [51]. Specifically, 2 mL of the electrolyte after N_2 reduction reaction was mixed with 2 mL of the color reagent (a mixture of 300 mL ethanol, 30 mL concentrated hydrochloric acid and 5.99 g para-(dimethylamino) benzaldehyde). All test solutions were incubated under darkness for 2 h before Ultraviolet-visible (UV-vis) tests. The absorption spectra between 400 and 550 nm for above mixture were measured by a UV-vis spectrophotometer, which exhibited an absorption peak at the wavelength of 458 nm. A series of reference solutions with suitable hydrazine monohydrate concentrations in 0.1 M Na_2SO_4 and 1 mM H_2SO_4 were used to plot standard concentration-absorbance curves.

2.6. Ammonia yield rate and faradaic efficiency calculation

The yield rate of ammonia can be calculated based on the following equation:

$$\text{NH}_3 \text{ Yield rate} = \frac{C_{\text{NH}_3} \times V}{t \times S} \quad (1)$$

The Faradaic efficiency (FE) refers to the percentage of the charge consumed for ammonia production compared to the total charge passed through the electrode, which can be calculated as follows:

$$\text{FE} = \frac{3F \times C_{\text{NH}_3} \times V}{17Q} \quad (2)$$

where C_{NH_3} is the measured ammonia concentration ($\mu\text{g mL}^{-1}$); V is the volume of 0.1 M Na_2SO_4 electrolyte or acid trap (L), t is the electrolysis time (2 h); S is the area of catalyst (typically $1 \times 1 \text{ cm}^2$); F is the Faradaic constant ($96,485 \text{ C mol}^{-1}$); and Q is the total charge passed through the electrode (C). According to the measurement results of three separately prepared samples under the same conditions, the ammonia yield rate, Faradaic efficiency, and error bar were determined.

2.7. In situ -FTIR measurement

The electrochemical in situ Fourier transform infrared (in situ-FTIR) experiments were carried out on a Nicolet iS 50 spectrometer equipped with a liquid nitrogen-cooled MCT-A detector. A ZnSe face-angled crystal with incident angle 60° was used as reflection element, and 64 scans, with a resolution of 4 cm^{-1} , were performed for each spectrum. The pressure-tight H-type cell was used to perform nitrogen reduction reaction, in which $\text{NiCoP/CoMoP/Co(Mo}_3\text{Se}_4)_4 @\text{C/NF}$ electrocatalyst, Ag/AgCl/ sat. KCl and platinum foil ($1 \times 1 \text{ cm}^2$) were used as the working, reference and counter electrode, respectively. The N_2 -saturated 0.1 M Na_2SO_4 was used as electrolyte. The Chronopotentiometry measurement was set in this experiment at -0.2 V vs RHE.

2.8. Density functional theory (DFT) calculations

All the spin-polarized density functional theory (DFT) computations were performed using the Dmol³ software package based on the linear combination of atomic orbitals (LCAO) method [52]. Electron-ion interactions were described using the DFT Semi-core Pseudopotops (DSPP) pseudopotentials. The Double Numerical plus p-functions (DND) basis set was employed to expand the wave functions with an orbital cutoff of 4.0 Å for Ni, 4.1 Å for Co, 3.7 Å for P, 3.8 Å for Se, 4.4 Å for Mo, 3.2 Å for N and 3.0 Å for H. For the electron-electron exchange and correlation interactions, the functional parametrized by Perdew-Burke-Ernzerhof (PBE), a form of the general gradient approximation (GGA), was used throughout. The Vander Waals interaction was described using the DFT-D2 method that proposed by Grimme [53].

The surface of the lattice was simulated with the slab model and a sufficiently large vacuum region of 15 Å was used to separate the peri-

odic images. During the geometry optimizations, the bottom atoms were fixed at the bulk position. In this work, the Brillouin-zone integrations were conducted using Monkhorst-Pack (MP) grids of special points. A k -point sets with a separation of 0.07 \AA^{-1} was used. The convergence criterion for the electronic self-consistent field (SCF) loop was set to 10^{-5} . The atomic structures were optimized until the residual forces were below $0.004 \text{ Ha \AA}^{-1}$. Note that the NH_3 molecules were calculated in a $(10 \times 10 \times 10) \text{ \AA}^3$ box with the Gamma-point only k -point sets, and the Gibbs free energy of the proton was derived from the calculated H_2 molecules via the computational hydrogen electrode (CHE). The Gibbs free energy (ΔG) of the absorbed species can be calculated by:

$$\Delta G = \Delta E + \Delta E_{ZPE} - T\Delta S + eU + \Delta G_{PH} \quad (3)$$

Where, ΔE is the reaction energy difference between the reactants and the products, ΔZPE is the zero-point energy change, ΔS is the entropy change, T is the finite temperature, e and U are the charge transferred and the applied potential, respectively, ΔG_{PH} is the correction free energy of H^+ . The zero-point energy and the entropy change were calculated from vibrational frequencies.

3. Results and discussion

3.1. Electrocatalyst synthesis and physical characterization

The facile two-step preparation strategy for the $\text{NiCoP}/\text{CoMoP}/\text{Co}(\text{Mo}_3\text{Se}_4)_4 @\text{C/NF}$ catalysts is clearly depicted in Fig. 1a. The $\text{NiCoMo-OH-urea}/\text{NF}$ products on the nickel foam ($\text{NiCoMo-OH-urea}/\text{NF}$) were initially fabricated via the solvo thermal method as precursor template, and then phosphorus and selenium sources were introduced simultaneously by calcination of their precursors. The colour change from

purple to black directly reflects the change in structural components before and after calcination, and the optical pictures of the synthesized samples are shown in Fig. S1.

As observed in scanning electron microscope (SEM) and atomic force microscope (AFM) images, the $\text{NiCoP}/\text{CoMoP}/\text{Co}(\text{Mo}_3\text{Se}_4)_4 @\text{C/NF}$ catalysts possess a flower-like nanosheet morphology with a thickness of approximately 100 nm and the crystal surface is relatively rough, which is conducive to enlarge the catalytic surface area and create more active sites (Fig. 1b–1d). The line-scan profile results further demonstrate that the $\text{NiCoP}/\text{CoMoP}/\text{Co}(\text{Mo}_3\text{Se}_4)_4 @\text{C/NF}$ has a three-layer wrapped structure, with Mo, Se, Ni, Co, P elements in the center; Co, Ni and P elements in the middle layer; and C element in the outer layer (Fig. 1e). The results are consistent with the energy-dispersive X-ray spectroscopy (EDX) element mappings (Fig. 1f). Additionally, high-resolution transmission electron microscope (HRTEM) characterization was performed. As shown in Fig. 1g–1h and Fig. S2, the well-resolved lattice fringes with interplanar distances of 0.26 nm, 0.29 nm and 0.19 nm corresponds to the (332) crystal plane of $\text{Co}(\text{Mo}_3\text{Se}_4)_4$, (110) plane of NiCoP and (212) plane of CoMoP [54], respectively, and obvious phase boundaries can be observed between them. This result indicates that triple heterojunction interfaces are simultaneously formed between different compositions ($\text{Co}(\text{Mo}_3\text{Se}_4)_4$ - NiCoP , NiCoP - CoMoP , and CoMoP - $\text{Co}(\text{Mo}_3\text{Se}_4)_4$), evidencing the existence of abundant distortions and lattice mismatches in the catalysts. Then, through the weight fraction of each element in the SEM-EDS results, the mass percentages of $\text{Co}(\text{Mo}_3\text{Se}_4)_4$, NiCoP and CoMoP were approximately calculated to be 51.1%, 38.7% and 10.2%, respectively (Fig. S3 and Tables S1–S2). Therefore, the heterostructures arrayed with triple interfaces are successfully achieved and the formed ordered 3D-array with strong mechanical strength and highly exposed structure. At the same time, the strong multi-interface coupling can adjust the electronic structure of $\text{NiCoP}/\text{CoMoP}/\text{Co}(\text{Mo}_3\text{Se}_4)_4 @\text{C/NF}$,

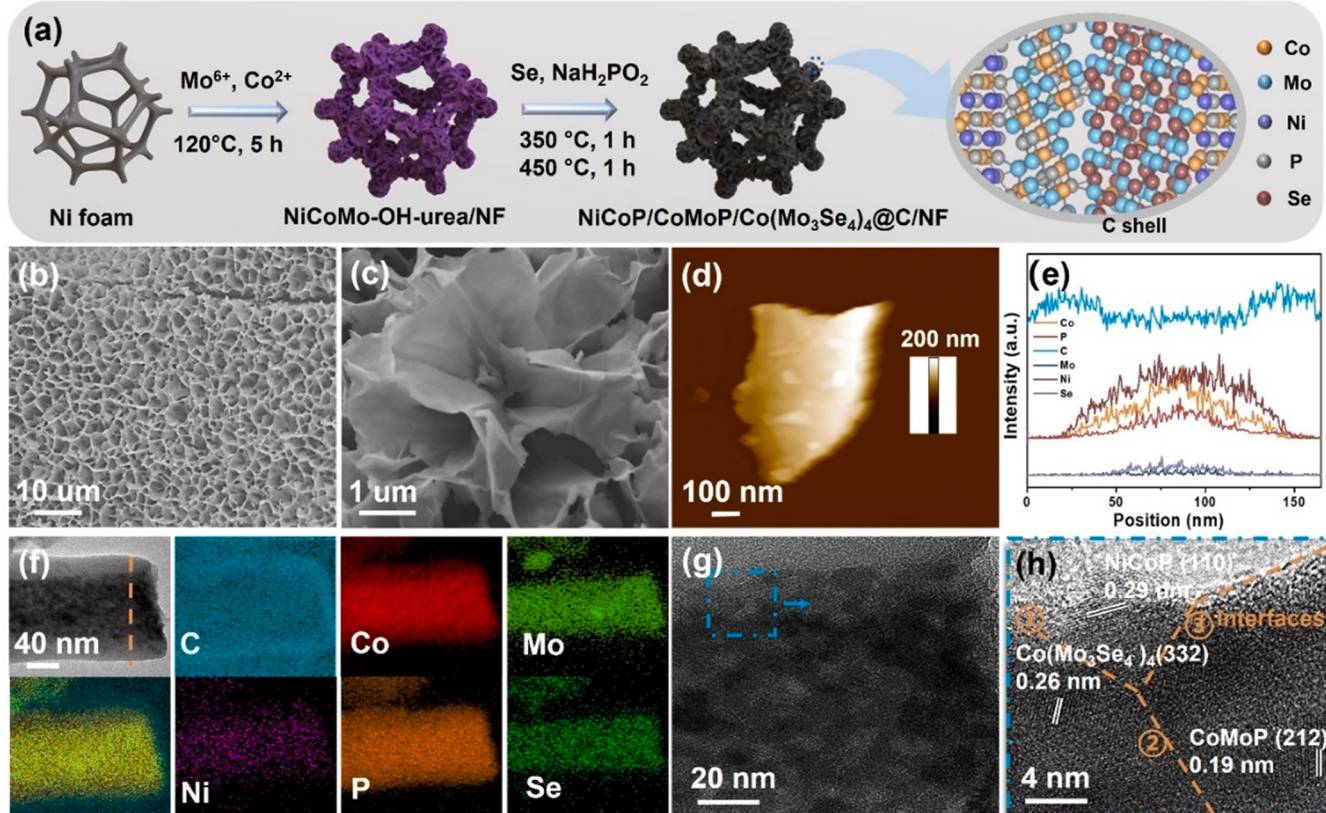


Fig. 1. Preparation and characterization of $\text{NiCoP}/\text{CoMoP}/\text{Co}(\text{Mo}_3\text{Se}_4)_4 @\text{C/NF}$. (a) Schematic illustration for the two-step synthesis of $\text{NiCoP}/\text{CoMoP}/\text{Co}(\text{Mo}_3\text{Se}_4)_4 @\text{C/NF}$. (b–c) SEM images. (d) AFM image. (e) Line-scan profile. (f) TEM image and corresponding EDX element mapping. (g) High-magnified TEM image and (h) HRTEM image.

leading to significantly enhanced NRR performance. For comparisons, the pure CoMoP and $\text{Co}(\text{Mo}_3\text{Se}_4)_4$ nanosheet arrays and pure NiCoP nanowire array on Ni foam were also synthesized in this work. The detailed physical characterizations are presented in Fig. S4–S6.

The nanocrystalline natures of the catalysts were confirmed by X-ray diffraction (XRD) (Fig. S7a and Fig. S7b). For NiCoP/CoMoP/Co $(\text{Mo}_3\text{Se}_4)_4$ @C/NF, except for the substrate peaks from Ni foam, the peaks centered at 33.6° and 37.1° are respectively attributed to the (332) and (20–2) planes of $\text{Co}(\text{Mo}_3\text{Se}_4)_4$, and the peaks located at 30.6° and 41.0° are respectively indexed to the (110) and (111) planes of NiCoP (JCPDS: 71–2336), while the peaks at 47.8° and 51.1° corresponding to the (212) and (203) planes of CoMoP (JCPDS: 32–0299), respectively. Thus, the characteristic diffraction peaks are related to NiCoP, CoMoP, and $\text{Co}(\text{Mo}_3\text{Se}_4)_4$, which are consistent with the results of HRTEM. For the XRD patterns of the as-prepared samples with different $\text{Na}_2\text{MoO}_4 \cdot 2 \text{H}_2\text{O}$ concentrations (Fig. S7c), although there are some differences in peak shape and peak strength, no obvious change in the peak position is observed. Therefore, the structure of the electrocatalysts does not vary with the $\text{Na}_2\text{MoO}_4 \cdot 2 \text{H}_2\text{O}$ concentration.

To explore the surface composition and electronic states of the NiCoP/CoMoP/Co $(\text{Mo}_3\text{Se}_4)_4$ @C/NF catalysts, the X-ray photoelectron spectroscopy (XPS) test was performed. XPS survey spectra show that NiCoP/CoMoP/Co $(\text{Mo}_3\text{Se}_4)_4$ @C/NF surface is mainly composed of Mo, Co, Ni, Se, and P and C elements. Fig. 2a presents the high-resolution Co 2p spectra of NiCoP/CoMoP/Co $(\text{Mo}_3\text{Se}_4)_4$ @C/NF. Two obvious peaks located at 793.3 and 778.3 eV well match the Co-P bond of Co 2p_{1/2} and Co 2p_{3/2}, respectively. Moreover, the peaks centered at 797.8 and 782.0 eV can be assigned to the Co oxidation species, while the peaks at 803.1 and 786.4 eV belong to the related satellite peaks [55]. Additionally, the peaks of the Co 2p_{1/2} and Co 2p_{3/2} in the NiCoP/CoMoP/Co $(\text{Mo}_3\text{Se}_4)_4$ @C/NF show a positive shift compared with that of the pure-Co $(\text{Mo}_3\text{Se}_4)_4$. Similarly, the XPS spectra of Mo 3d including Mo 3d_{3/2} and Mo 3d_{5/2} report slight positive shift to higher binding energies (Fig. 2b). Fig. 2c shows Ni 2p spectrum including Ni 2p_{3/2} and Ni 2p_{1/2}. The peaks at 852.6 and 869.4 eV, 856.0 and 873.5 eV, 861.4 and 879.6 eV respectively attributed to Ni-P, oxidized Ni species as well as the satellite peaks, indicating the existence of NiCoP and CoMoP. Similarly, the XPS peaks of Ni-P exhibit slight positive shift to higher binding energies [56–58]. In sharp contrast, for the high-resolution Se 3d spectra of NiCoP/CoMoP/Co $(\text{Mo}_3\text{Se}_4)_4$ @C/NF, the peaks of Se 3d_{5/2} and Se 3d_{3/2} located at binding energies of 54.2 and 55.3 eV exhibit negative shift relative to that of pure-Co $(\text{Mo}_3\text{Se}_4)_4$, as shown in Fig. 2d [59–61]. The above shifts of binding energy readily elucidate that the charge redistribution occurs due to the strong interaction at the interface of the NiCoP and CoMoP in Co $(\text{Mo}_3\text{Se}_4)_4$, which could significantly enhance the NRR performance [62]. Besides, to further explore the

effect of phosphating on the catalysts before and after P doping (Fig. S8), the XPS test for C 1 s was performed. Interestingly, the C 1 s spectra show a 0.5 eV negative shift after the addition of P, reflecting more enriched electrons in the carbon layer [63]. This result indicates that the P modification can provide faster charge transfer from the internal metal compounds to the carbon layer, further improving the electrocatalytic activity.

3.2. Electrochemical properties

The electrocatalytic performance of the 3D-networked NiCoP/CoMoP/Co $(\text{Mo}_3\text{Se}_4)_4$ @C/NF for NRR was measured in 0.1 M Na_2SO_4 electrolyte using a standard H-type cell separated by a proton exchange membrane (Nafion 211), in which self-supporting nanoflowers with dimensions of 1 cm × 1 cm was directly utilized as the work electrode (Fig. S9). We initially performed linear sweep voltammetry (LSV) tests in an Ar-saturated and N_2 -saturated electrolyte to qualitatively distinguish between HER and NRR, respectively. Obviously, a higher current density can be observed between -0.10 V and -0.35 V (vs. RHE) under the N_2 atmosphere, indicating the possibility of the as-prepared NiCoP/CoMoP/Co $(\text{Mo}_3\text{Se}_4)_4$ for use as effective NRR electrocatalysts at room temperature and atmospheric pressure (Fig. S10a). Then, a series of chronoamperometry (CA) tests at different applied potentials [-0.10 , -0.15 , -0.20 , -0.25 , -0.30 , -0.35 V (vs. RHE)] were conducted to determine the ammonia yield rates and Faradaic efficiencies (Fig. S10b) [64]. As shown in Fig. 3a, the electrochemical NRR obtains the highest activity and selectively at the potential of -0.2 V vs. RHE, with the ammonia yield of $24.54 \mu\text{g h}^{-1} \text{cm}^{-2}$ and corresponding Faradaic efficiency of 23.15% (detecting calibration curve for colorimetric ammonia shown in Fig. S11), surpassing that of most reported transition bimetal-based electrocatalysts (Table S3). Meanwhile, the absence of byproduct N_2H_4 indicates the excellent selectivity of NiCoP/CoMoP/Co $(\text{Mo}_3\text{Se}_4)_4$ @C/NF catalysts for NRR, as shown in Fig. S13 (detecting calibration curve for colorimetric hydrazine shown in Fig. S12). Moreover, as the applied potential becomes more negative, both NH_3 yield rate and corresponding Faradaic efficiency decrease considerably (NH_3 yield rate: $3.41 \mu\text{g h}^{-1} \text{cm}^{-2}$, Faradaic efficiency: 0.39% at -0.35 V vs. RHE), revealing that HER is the dominant reaction at the cathode. To verify the deduction that the measured ammonia comes indeed from electrochemical NRR rather than from any nitrogenous contaminants from the environment (e.g., membrane, cell, nitrogen gas, laboratory), extensive control experiments were carried out in this work, including Ar-saturated electrolyte, bare Ni foam without catalyst, open circuit, or Na_2SO_4 electrolyte placed in the air for 24 h. All results demonstrate that there is no detectable NH_3 production (Fig. 3b). To further confirm the origin of NH_3 , we performed isotope labeling experiments by using $^{15}\text{N}_2$

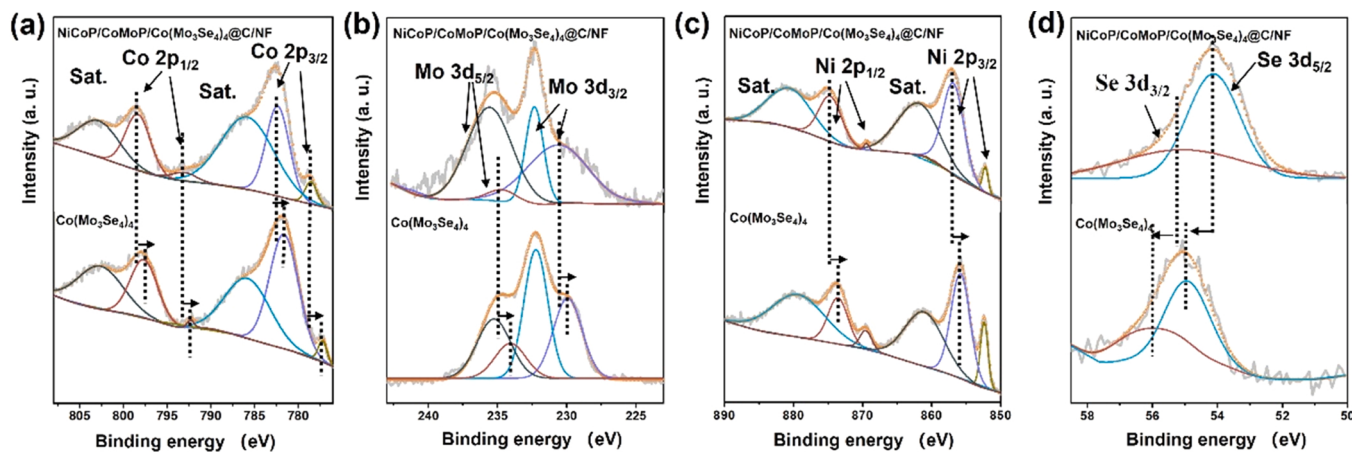


Fig. 2. Structural and chemical identification of NiCoP/CoMoP/Co $(\text{Mo}_3\text{Se}_4)_4$ @C/NF and pure- $\text{Co}(\text{Mo}_3\text{Se}_4)_4$. (a) Co 2p XPS spectra. (b) Mo 3d XPS spectra. (c) Ni 2p XPS spectra. (d) Se 3d XPS spectra.

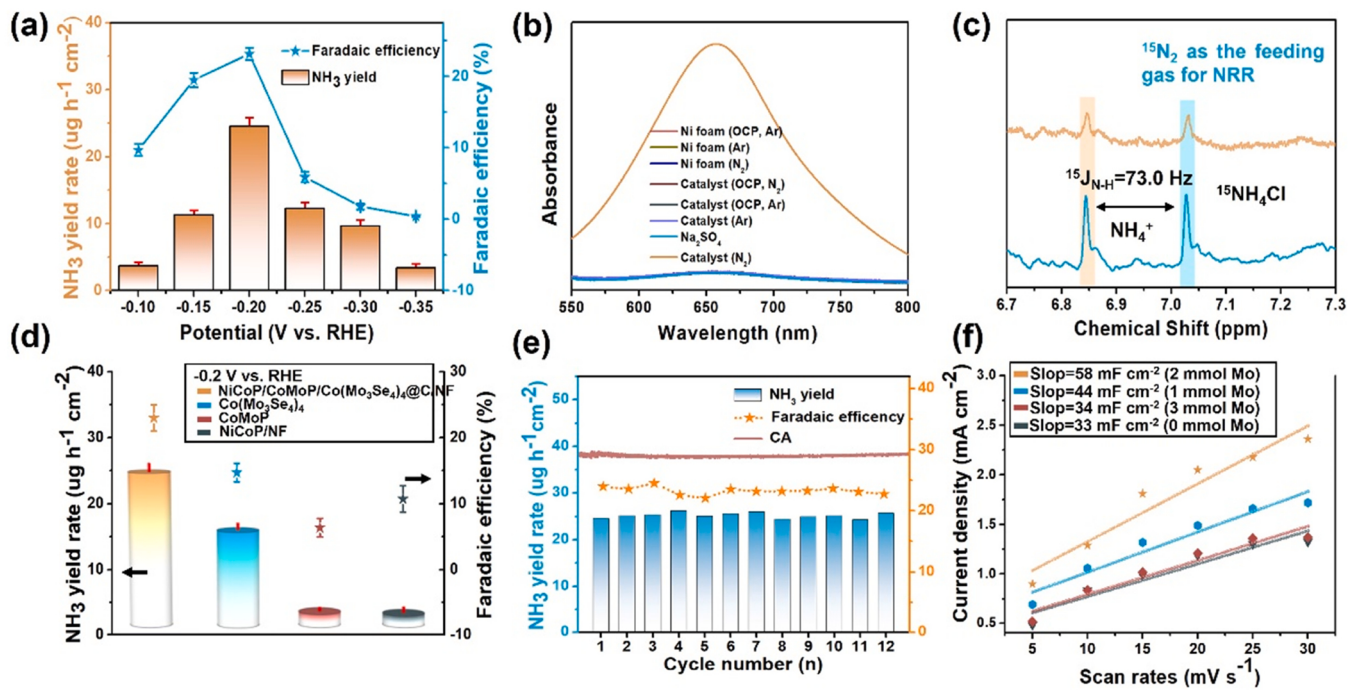


Fig. 3. Electrochemical nitrogen reduction activities of NiCoP/CoMoP/Co(Mo₃Se₄)₄ @C/NF. (a) NH₃ yield rates and Faradaic efficiencies of NiCoP/CoMoP/Co(Mo₃Se₄)₄ @C/NF at each given potential. The error bars correspond to the standard deviations of measurements over six separately prepared samples under the same conditions. (b) Ultraviolet-visible absorption spectra of electrolytes stained with indophenol blue indicator after NRR on catalysts, Ni foam, Ar control experiment, open circuit condition at –0.2 V vs. RHE, and Na₂SO₄ solution placed in the air for 24 h. (c) ¹H NMR spectra (400 MHz) of ¹⁵NH₄⁺ produced from the NRR reaction (at –0.2 V vs. RHE) using ¹⁵N₂ as the N₂ source. (d) NH₃ yield rates and Faradaic efficiencies of NiCoP/CoMoP/Co(Mo₃Se₄)₄ @C/NF, NiCoP/NF, CoMoP and Co(Mo₃Se₄)₄. (e) Cycling stability results at –0.2 V vs. RHE. (f) Electrochemically active surface area measurement results for NiCoP/CoMoP/Co(Mo₃Se₄)₄ @C/NF with different Na₂MoO₄ concentrations.

as the feeding gas, and the ¹H nuclear magnetic resonance (NMR) spectra shows doublet peaks with the coupling constants of 73.0 Hz (Fig. 3c), which is assigned to the standard ¹⁵NH₄⁺ sample (Fig. S14).

In order to illustrate the effect of multi-heterojunction structures of catalysts in the NRR, comparative samples (pure-Co(Mo₃Se₄)₄, pure-CoMoP, NiCoP/NF) were used for the N₂ reduction tests in this work (Fig. 3d). Strikingly, the NH₃ yield rate (24.54 μg h⁻¹ cm⁻²) and Faradaic efficiency (23.15%) of NiCoP/CoMoP/Co(Mo₃Se₄)₄ @C/NF are far better than that of the pure-Co(Mo₃Se₄)₄ (15.33 μg h⁻¹ cm⁻², 16.50%), pure-CoMoP (2.12 μg h⁻¹ cm⁻², 0.96%) and NiCoP/NF (1.84 μg h⁻¹ cm⁻², 1.02%) (Fig. S15), which reveal that the pure-Co(Mo₃Se₄)₄ requires lower energy barrier for the rate-determining step to facilitate NRR. Therefore, we can infer that when NiCoP/CoMoP/Co(Mo₃Se₄)₄ @C/NF as the working electrode, Co(Mo₃Se₄)₄ are more likely act as the main active site to activate N₂ efficiently. To further explore the charge transfer phenomenon at the electrocatalysts reaction interface, we performed electrochemical impedance spectroscopies (EIS) tests for the as-synthesized NiCoP/CoMoP/Co(Mo₃Se₄)₄ @C/NF, Co(Mo₃Se₄)₄, CoMoP and NiCoP/NF in a three-electrode system, respectively. Charge transfer resistance (R_{ct}) were calculated and compared according to the corresponding equivalent circuit values from Nyquist curves. The diameter of each semicircle in Nyquist diagram reflects the charge transfer resistance of as-synthesized electrocatalysts and smaller value indicates faster charge-transfer capability and higher conductivity. As shown in the Fig. S16, EIS results demonstrate that the lower charge-transfer resistance is noticed for the NiCoP/CoMoP/Co(Mo₃Se₄)₄ @C/NF (18 Ω) compared to that of the Co(Mo₃Se₄)₄ (24 Ω), CoMoP (40 Ω) and NiCoP/NF (52 Ω). These results reveal that the synergistic effect of the multi-heterojunctions could play a decisive role for the exceptional electron-transfer behavior during the electrochemical reaction and excellent NRR performance. Experiments were also performed to measure the produced NH₃ and corresponding

Faradaic efficiencies at a constant potential of –0.2 V vs. RHE with N₂ flow rates in a range of 10–100 sccm. As shown in Fig. S17, when the N₂ flow rate is lower than 20 sccm, the NRR reaction rate is below the optimal value due to insufficient N₂ supply. When the flow rate is greater than 20 sccm, the supply of N₂ is no longer a limiting factor for the NRR. On the contrary, an exceedingly high flow rate can be unfavorable to the formation of the optimal three-phase interfacial structure, leading to a poor reaction effect. Therefore, the appropriate N₂ flow rate is critical for the NRR. In addition, the durability and stability are the key performance indicators for electrocatalyst used for practical application. The cyclic chronoamperometric test results (Fig. 3e) show that high NH₃ yield rate is maintained after 12 repeated cycles and no obvious fluctuation in the current intensity is observed during the long-term nitrogen reduction process. To avoid the adsorption of ammonia on the catalysts surface from the previous cycle test, one control experiment was performed by alternating bubbled N₂ or Ar every 2 h into 0.1 M Na₂SO₄ electrolyte at –0.2 V vs. RHE for up to 10 h. As shown in Fig. S18, NH₃ was only measured in the periods of N₂-saturated electrolyte, demonstrating good cycling stability. Moreover, the structural and morphological stabilities of the catalyst were also evaluated by the SEM, TEM, XPS and XRD tests after 24 h of NRR operation. As shown in the Fig. S19 and Fig. S20, no significant changes in the SEM and TEM images after NRR, demonstrating that the NiCoP/CoMoP/Co(Mo₃Se₄)₄ @C/NF had superb heterostructure stability as its well-maintained architecture. Additionally, XRD and XPS analysis reveal that no obvious peaks shift or change of valence states of Co, Mo, Ni and Se were observed after the NRR process, due to the synergistic effect of the strong interface interaction in the heterostructure.

To explore the relationship between the Na₂MoO₄·2 H₂O concentration and the morphology and properties of the electrocatalysts, NiCoP/CoMoP/Co(Mo₃Se₄)₄ @C/NF catalysts with different Na₂MoO₄·2 H₂O concentrations (0, 1, 2, 3 mM) were prepared. As

shown in Fig. S21, the NiCoP/CoMoP/Co(Mo_3Se_4)₄ @C/NF with 2 mM $\text{Na}_2\text{MoO}_4 \cdot 2 \text{H}_2\text{O}$ exhibits the best NRR performance, which is possibly due to the structure that can expose more active sites. As revealed in the SEM images in Fig. S22, the prepared sample shows needle-like nanowire morphology in the absence of $\text{Na}_2\text{MoO}_4 \cdot 2 \text{H}_2\text{O}$; and more flower-like nanosheets are formed as the $\text{Na}_2\text{MoO}_4 \cdot 2 \text{H}_2\text{O}$ concentration increases. When the amount of $\text{Na}_2\text{MoO}_4 \cdot 2 \text{H}_2\text{O}$ is 1 mM, the nanosheet array is relatively sparse and thick, resulting in a small specific surface area. When the concentration of $\text{Na}_2\text{MoO}_4 \cdot 2 \text{H}_2\text{O}$ increases to 3 mM, some nanosheets aggregate together to form spheres, which limit the exposure of the active sites and such phenomenon is not conducive to adsorption and desorption of intermediates and diffusion of electrolyte. However, when the concentration of $\text{Na}_2\text{MoO}_4 \cdot 2 \text{H}_2\text{O}$ is 2 mM, the nanoflowers are formed with thin sheets and sufficiently rough surfaces, resulting in favorable exposure of active sites for nitrogen fixation. It is known that the improvement of morphology is usually closely related to electrochemically active surface area (ECSA). As shown in Fig. 3f and Fig. S23, NiCoP/CoMoP/Co(Mo_3Se_4)₄ @C/NF exhibits the largest ECSA, further confirming that the introduction of Mo can create more active sites and enhance the NRR performance of the catalysts.

3.3. In situ-FTIR experiments and analysis

Electrochemical in situ Fourier transform infrared spectroscopy (in situ-FTIR) is a powerful tool to analyze the complex reaction mechanism of nitrogen reduction by monitoring the presence and identities of intermediates. Fig. 4a and 4b depict time-resolved in situ-FTIR spectra collected on the catalyst surface in a chronoamperometry scan at -0.2 V vs. RHE in N_2 -saturated 0.1 M Na_2SO_4 for 1440 s, where the time interval between two successive spectra is 180 s. It is clear that the absorption band at 1113 cm^{-1} is attributed to the N-N stretching and the peak intensity increases with the extension of reaction time, indicating that the $\text{N}\equiv\text{N}$ triple bond is cleaved into a single bond. In addition, two obvious absorption signals at 1303 and 1457 cm^{-1} observed are assigned to $-\text{NH}_2$ wagging and H-N-H bending, respectively.

Simultaneously, two minor adsorption bands located at 1380 and 1685 cm^{-1} respectively correspond to the asymmetric and symmetric deformation vibration of $\delta_{as}\text{NH}_4^+$ and $\delta_s\text{NH}_4^+$ generated during the nitrogen reduction reaction. Finally, two unignorable absorption bands centered at ~ 3360 and $\sim 2965 \text{ cm}^{-1}$ detected are attributed to the N – H stretching of ammonia in the solution [65]. These signals can be clearly revealed in a single spectrum shown in Fig. 4c. In sharp contrast, no such obvious signals are observed in the electrochemical in situ FTIR spectrum obtained in Ar-saturated 0.1 M Na_2SO_4 (black line), affirming the detected ammonia originates from nitrogen reduction reaction rather than nitrogenous contaminants, in consistence with the NMR result. Therefore, according to the above in situ FTIR observations, it can conclude that the NRR on NiCoP/CoMoP/Co(Mo_3Se_4)₄ @C/NF follows an alternating pathway (Fig. 4d). Specially, the dissolved N_2 molecules can be initially adsorbed by the positively charged metals (Ni, Co and Mo) surface sites on NiCoP/CoMoP/Co(Mo_3Se_4)₄ @C/NF due to the charge transfer from transition metals to non-metal (P and Se) sites. The negatively charged P and Se active sites turn into anchoring points for H^+ from H_2O through hydrogen bonding. Then, the activated H^+ favor to form a highly stable $-\text{N}\equiv\text{N}-\text{H}$ bond, which can accelerate the dissociation of $\text{N}\equiv\text{N}$ bond. Next, another H^+ hydrogenates the weakened $-\text{N}\equiv\text{N}-\text{H}$ to form a $-\text{H}-\text{N}=\text{N}-\text{H}$ bond; thereafter, a free NH_3 molecule associated with the adsorbed $-\text{NH}_2$ is generated by continuous electron transfer and hydrogenation. Finally, the second NH_3 molecule is obtained by adding the H^+ and electron to $-\text{NH}_2$, indicating that a complete nitrogen reduction reaction is achieved on the NiCoP/CoMoP/Co(Mo_3Se_4)₄ @C/NF surface under ambient temperature and normal atmospheric pressure (Photograph of the in situ FTIR measurement as shown in Fig. S24).

3.4. DFT calculations and analysis

To better interpret the synergistic mechanism at the triple-hybrid interfaces for enhancing NRR activity, a series of density functional theory (DFT) computations were performed on the NiCoP/CoMoP/Co

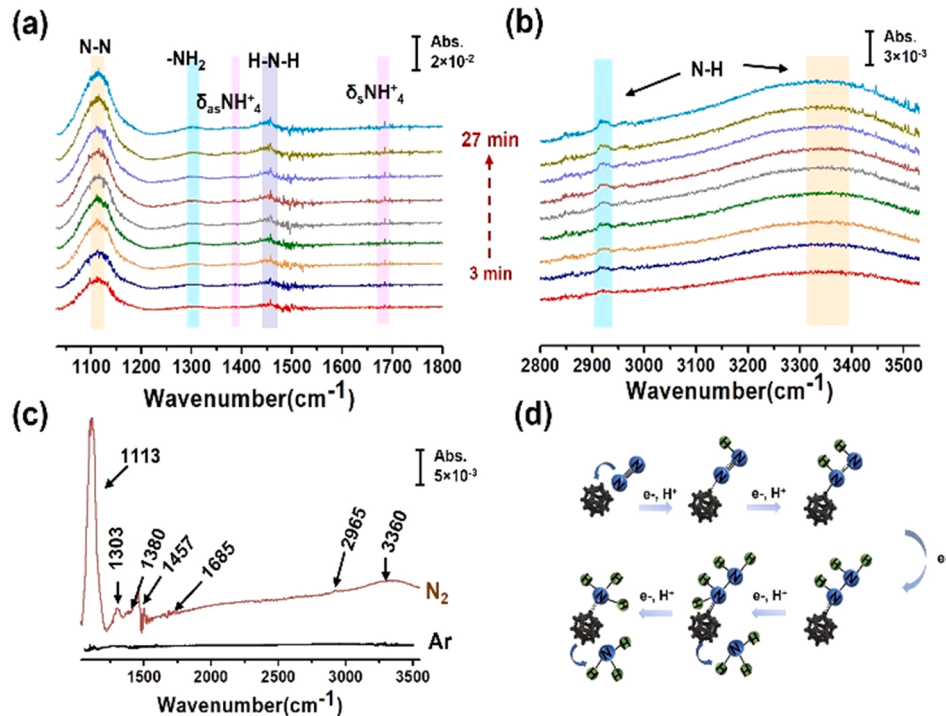


Fig. 4. Electrochemical in situ-FTIR spectra of the NRR. (a, b) Electrochemical in situ-FTIR spectra of the NRR on the NiCoP/CoMoP/Co(Mo_3Se_4)₄ @C/NF electrode at -0.2 V vs. RHE under N_2 -bubbled 0.1 M Na_2SO_4 . (c) The single in situ-FTIR spectrum at -0.2 V vs. RHE in the range of 1050 – 3600 cm^{-1} . (d) Nitrogen electrochemical reduction reaction pathway on NiCoP/CoMoP/Co(Mo_3Se_4)₄ @C/NF surface.

$(\text{Mo}_3\text{Se}_4)_4$, NiCoP/CoMoP, CoMoP/Co $(\text{Mo}_3\text{Se}_4)_4$ and NiCoP/Co $(\text{Mo}_3\text{Se}_4)_4$ systems. The model configurations are presented in Fig. S25–S28. In particular, based on the in-situ FTIR results, we explored the subsequent NRR steps through the alternating pathway, in which nitrogen adsorption, six-proton transferred were involved. The calculated Gibbs free energy of each intermediate during the NRR process on NiCoP/CoMoP/Co $(\text{Mo}_3\text{Se}_4)_4$, NiCoP/CoMoP, CoMoP/Co $(\text{Mo}_3\text{Se}_4)_4$ and NiCoP/Co $(\text{Mo}_3\text{Se}_4)_4$ systems is shown in Fig. 5a. The computational results show that the hydrogenation step ($^*\text{N}_2$ to $^*\text{N}_2\text{H}$) is the rate-determining step for all of the systems, while NiCoP/CoMoP/Co $(\text{Mo}_3\text{Se}_4)_4$ exhibits a lower energy barrier with 0.58 eV. The results evidence that, compared with the electrocatalyst with a single heterojunction, the synergistic effect of triple heterojunctions facilitates NRR by lowering the energy barrier for the rate-determining step, in consistency with the experimental observation that NiCoP/CoMoP/Co $(\text{Mo}_3\text{Se}_4)_4$ demonstrates better NRR performance.

We next carefully analyzed the actual roles of every component (NiCoP, CoMoP, Co $(\text{Mo}_3\text{Se}_4)_4$) and their interfaces in modulating electronic structure of NiCoP/CoMoP/Co $(\text{Mo}_3\text{Se}_4)_4$ and boosting NRR activity. The Electrostatic potential map and charge population analysis (Fig. S29 and Fig. 5b) illustrate that there are electron migrations from NiCoP and CoMoP to Co $(\text{Mo}_3\text{Se}_4)_4$ across their contact interfaces, leading to an electron accumulation on Co $(\text{Mo}_3\text{Se}_4)_4$ but electron depletions on CoMoP and NiCoP, in consistence with the XPS results. These results indicate that the charge accumulation induced by the heterojunction interfaces can facilitate the N_2 adsorption and spin polarization on the catalyst, thereby promoting the potential-determining step of the first protonation to form $^*\text{NNH}$. In this work, the work function calculations were also performed for NiCoP, CoMoP and Co $(\text{Mo}_3\text{Se}_4)_4$. However, the average potential profiles disclose that Co $(\text{Mo}_3\text{Se}_4)_4$ exhibits a smaller work function than NiCoP (Fig. 5c), but the electrons are transferred from NiCoP to Co $(\text{Mo}_3\text{Se}_4)_4$. Therefore, we can infer that the decoration of CoMoP can be used as an electron carrier to transfer electrons from NiCoP to Co $(\text{Mo}_3\text{Se}_4)_4$, playing the same role of Fe₈S₇ in nitrogenase. In addition, the calculated density of the states (DOS) demonstrates that the NiCoP/CoMoP/Co $(\text{Mo}_3\text{Se}_4)_4$ heterostructure is in the metallic state with an enhanced carrier density near the Fermi level

(Fig. 5d), compared with that of NiCoP/CoMoP, CoMoP/Co $(\text{Mo}_3\text{Se}_4)_4$ and NiCoP/Co $(\text{Mo}_3\text{Se}_4)_4$. Hence, the electron redistribution induced by the triple heterostructure electron coupling leads to a higher electrical conductivity and contributes to a high interconnectivity to enable elevated charge transfer for an efficient electrocatalytic reaction. Based on the above results, we can conclusion that: (1) NiCoP as the electron donor can interact with the triple bond of nitrogen molecules and facilitates the adsorption of nitrogen in the electrolyte; (2) CoMoP is responsible for transferring electrons to the Co $(\text{Mo}_3\text{Se}_4)_4$ from the NiCoP; (3) Co $(\text{Mo}_3\text{Se}_4)_4$ functions as the electron acceptor and also as the key active site to catalytic reduction of nitrogen; (4) the coexistence of triple interfaces can induce more effective electron redistribution and optimize free energies of intermediates; (5) The presence of C shell can further improve the conductivity and mechanical stability of NiCoP/CoMoP/Co $(\text{Mo}_3\text{Se}_4)_4$. The above analysis also explains why NiCoP/CoMoP/Co $(\text{Mo}_3\text{Se}_4)_4$ can decrease the energy barrier of hydrogenation steps and improve the activity and selectively of NRR.

4. Conclusions

In summary, herein we present and describe the successful design of NiCoP/CoMoP/Co $(\text{Mo}_3\text{Se}_4)_4$ @C/NF as inexpensive but effective transition metal electrocatalysts to reduce gaseous dinitrogen under ambient conditions, which demonstrate great potential as commercial catalysts for large-scale industrial ammonia synthesis due to the simple preparation methods, inexpensive raw materials, and excellent activity and stability. The NRR performance reaches $24.54 \mu\text{g h}^{-1} \text{cm}^{-2}$ with a desirable Faradaic efficiency of 23.15%. More importantly, the triple heterojunction interfaces among NiCoP, CoMoP and Co $(\text{Mo}_3\text{Se}_4)_4$ tune the electronic structure of electrocatalysts for lowered energy barrier of intermediates in electrolyte to promote the NRR process. Simultaneously, the constructed bionic structures of NiCoP/CoMoP/Co $(\text{Mo}_3\text{Se}_4)_4$ @C/NF effectively control the electron transport for an improved ammonia yield rate. The above results introduce new dimensions for the application of interface engineering in electrocatalyst design, using appropriate strategies to control the composition distribution of the catalyst to achieve the coexistence of multiple

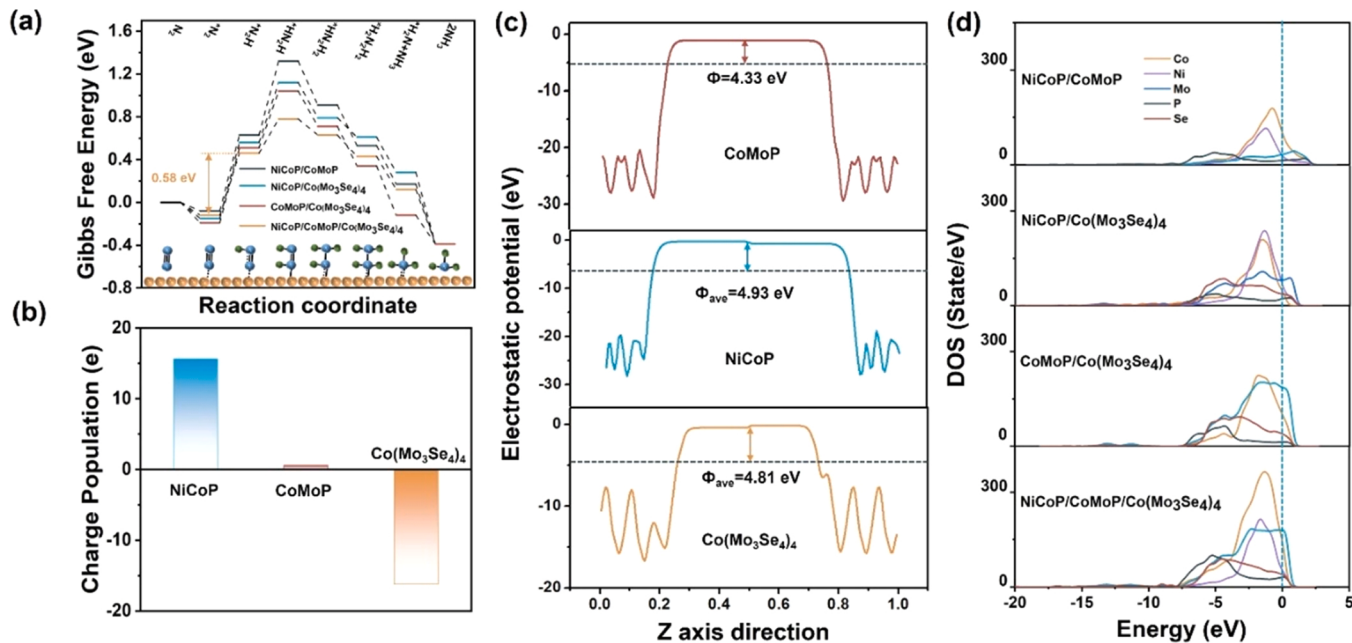


Fig. 5. DFT calculation results. (a) The calculated free energy diagram for NRR through the alternating mechanism on NiCoP/CoMoP, NiCoP/Co $(\text{Mo}_3\text{Se}_4)_4$, CoMoP/Co $(\text{Mo}_3\text{Se}_4)_4$ and NiCoP/CoMoP/Co $(\text{Mo}_3\text{Se}_4)_4$. (b) Charge population analysis of NiCoP, CoMoP and Co $(\text{Mo}_3\text{Se}_4)_4$ in the NiCoP/CoMoP/Co $(\text{Mo}_3\text{Se}_4)_4$. (c) Average potential profiles along the c-axis direction for determining work functions of NiCoP, CoMoP and Co $(\text{Mo}_3\text{Se}_4)_4$. (d) DOS of NiCoP/CoMoP, NiCoP/Co $(\text{Mo}_3\text{Se}_4)_4$, CoMoP/Co $(\text{Mo}_3\text{Se}_4)_4$ and NiCoP/CoMoP/Co $(\text{Mo}_3\text{Se}_4)_4$.

heterojunction interfaces, which can optimize specific reactions from low reactivity to high yield. This work motivates further research and provides a novel design route for other heterojunction engineered catalysts.

CRediT authorship contribution statement

Xin Li: Methodology, Investigation, Writing – original draft, Writing – review & editing. **Guangtong Hai:** Software. **Jin Liu:** Investigation. **Fenglin Zhaoa. Zehua Peng:** Investigation. **Honghong Liu:** Investigation. **Michael K.H. Leung:** Conceptualization, Methodology, Funding acquisition, Supervision. **Haihui Wang:** Conceptualization, Methodology, Writing – review & editing, Funding acquisition, Supervision. All authors discussed the results and commented on the manuscript.

Declaration of Competing Interest

The authors declare that they have no known competing financial interests or personal relationships that could have appeared to influence the work reported in this paper.

Acknowledgments

This work was financially supported by National Key Research and Development Program of China (Grant No. 2020YFB1505603), the Research Grants Council of the Hong Kong Special Administrative Region, China (Project No. CityU 11206520), National Natural Science Foundation of China (No. 22138005), Ningbo Municipal Government Innovation 2025 Scheme (No. 2018B10023) and the Shenzhen Knowledge Innovation Program (Basic Research, JCYJ20190808181205752).

Appendix A. Supporting information

Supplementary data associated with this article can be found in the online version at [doi:10.1016/j.apcatb.2022.121531](https://doi.org/10.1016/j.apcatb.2022.121531).

References

- [1] D. Bao, Q. Zhang, F. Meng, H. Zhong, M. Shi, Y. Zhang, J. Yan, Q. Jiang, X. Zhang, Electrochemical Reduction of N₂ under ambient conditions for artificial N₂ fixation and renewable energy storage using N₂/NH₃ cycle, *Adv. Mater.* 29 (2017), 1604799.
- [2] J.G. Chen, R.M. Crooks, L.C. Seefeldt, K.L. Bren, R.M. Bullock, M.Y. Daresbourg, P.L. Holland, B. Hoffman, M.J. Janik, A.K. Jones, M.G. Kanatzidis, P. King, K. M. Lancaster, S.V. Lymar, P. Pfromm, W.F. Schneider, R.R. Schrock, Beyond fossil fuel-driven nitrogen transformations, *Science* 360 (2018).
- [3] Y. Ma, T. Yang, H. Zou, W. Zang, Z. Kou, L. Mao, Y. Feng, L. Shen, S.J. Pennycook, L. Duan, X. Li, J. Wang, Synergizing Mo single atoms and Mo₂C nanoparticles on CNTs synchronizes selectivity and activity of electrocatalytic N₂ reduction to ammonia, *Adv. Mater.* 32 (2020), e2002177.
- [4] S. Liu, T. Qian, M. Wang, H. Ji, X. Shen, C. Wang, C. Yan, Proton-filtering covalent organic frameworks with superior nitrogen penetration flux promote ambient ammonia synthesis, *Nat. Cat.* 4 (2021) 322–331.
- [5] B.C. Stuart Licht, B. Cui, F. Wang, S. Li, J. Lau, S. Liu, Ammonia synthesis by N₂ and steam electrolysis in molten hydroxide suspensions of nanoscale Fe₂O₃, *Science* 345 (2020).
- [6] S.Z. Andersen, V. Colic, S. Yang, J.A. Schwalbe, A.C. Nielander, J.M. McEnaney, K. Enemark-Rasmussen, J.G. Baker, A.R. Singh, B.A. Rohr, M.J. Statt, S.J. Blair, S. Mezzavilla, J. Kibsgaard, P.C.K. Vesborg, M. Cargnello, S.F. Bent, T.F. Jaramillo, I.E.L. Stephens, J.K. Norskov, I. Chorkendorff, A rigorous electrochemical ammonia synthesis protocol with quantitative isotope measurements, *Nature* 570 (2019) 504–508.
- [7] L. Gao, Y. Cao, C. Wang, X. Yu, W.B. Li, Y. Zhou, B. Wang, Y. Yao, C. Wu, W. Luo, Z. Zou, Domino effect: gold electrocatalyzing lithium reduction to accelerate nitrogen fixation, *Angew. Chem. Int. Ed.* 60 (2021) 5257–5261.
- [8] S. Li, Y. Luo, L. Yue, T. Li, Y. Wang, Q. Liu, G. Cui, F. Zhang, A.M. Asiri, X. Sun, An amorphous WC thin film enabled high-efficiency N₂ reduction electrocatalysis under ambient conditions, *Chem. Commun.* 57 (2021) 7806–7809.
- [9] A.J. Martín, T. Shinagawa, J. Pérez-Ramírez, Electrocatalytic reduction of nitrogen: from haber-bosch to ammonia artificial leaf, *Chem* 5 (2019) 263–283.
- [10] N. Lazouski, M. Chung, K. Williams, M.L. Gala, K. Manthiram, Non-aqueous gas diffusion electrodes for rapid ammonia synthesis from nitrogen and water-splitting-derived hydrogen, *Nat. Cat.* 3 (2020) 463–469.
- [11] F. Jiao, B. Xu, Electrochemical ammonia synthesis and ammonia fuel cells, *Adv. Mater.* 31 (2019), e1805173.
- [12] Q. Liu, Y. Lin, L. Yue, J. Liang, L. Zhang, T. Li, Y. Luo, M. Liu, J. You, A.A. Alshehri, Q. Kong, X. Sun, Bi nanoparticles/carbon nanosheet composite: A high-efficiency electrocatalyst for NO reduction to NH₃, *Nano Res.* (2022).
- [13] B.H.R. Suryanto, H. Du, D. Wang, J. Chen, A.N. Simonov, D.R. MacFarlane, Challenges and prospects in the catalysis of electroreduction of nitrogen to ammonia, *Nat. Cat.* 2 (2019) 290–296.
- [14] X. Guo, J. Gu, S. Lin, S. Zhang, Z. Chen, S. Huang, Tackling the Activity and selectivity challenges of electrocatalysts toward the nitrogen reduction reaction via atomically dispersed bi atom catalysts, *J. Am. Chem. Soc.* 142 (2020) 5709–5721.
- [15] O. Einsle, D.C. Rees, Structural enzymology of nitrogenase enzymes, *Chem. Rev.* 120 (2020) 4969–5004.
- [16] J. Deborah, D. Harold, E. William, E. Kevin, Role for the nitrogenase MoFe protein a-subunit in FeMo-cofactor binding and catalysis, *Nature* 343 (1989).
- [17] Y. Hao, Y. Guo, L. Chen, M. Shu, X. Wang, T. Bu, W. Gao, N. Zhang, X. Su, X. Feng, J. Zhou, B. Wang, C. Hu, A. Yin, R. Si, Y. Zhang, C. Yan, Promoting nitrogen electroreduction to ammonia with bismuth nanocrystals and potassium cations in water, *Nat. Cat.* 2 (2019) 448–456.
- [18] H. Li, J. Shang, Z. Ai, L. Zhang, Efficient visible light nitrogen fixation with BiOBr nanosheets of oxygen vacancies on the exposed {001} facets, *J. Am. Chem. Soc.* 137 (2015) 6393–6399.
- [19] S. Zhang, M. Jin, T. Shi, M. Han, Q. Sun, Y. Lin, Z. Ding, L. Zheng, G. Wang, Y. Zhang, H. Zhang, H. Zhao, Electrocatalytically active Fe-(O-C₂)₄ single-atom sites for efficient reduction of nitrogen to ammonia, *Angew. Chem. Int. Ed.* 59 (2020) 13423–13429.
- [20] T. Wu, X. Zhu, Z. Xing, S. Mou, C. Li, Y. Qiao, Q. Liu, Y. Luo, X. Shi, Y. Zhang, X. Sun, Greatly improving electrochemical N₂ reduction over TiO₂ nanoparticles by iron doping, *Angew. Chem. Int. Ed.* 58 (2019) 18449–18453.
- [21] Y. Wang, M. Shi, D. Bao, F. Meng, Q. Zhang, Y. Zhou, K. Liu, Y. Zhang, J. Wang, Z. Chen, D. Liu, Z. Jiang, M. Luo, L. Gu, Q. Zhang, X. Cao, Y. Yao, M. Shao, Y. Zhang, X. Zhang, J. Chen, J. Yan, Q. Jiang, Generating defect-rich bismuth for enhancing the rate of nitrogen electroreduction to ammonia, *Angew. Chem. Int. Ed.* 58 (2019) 9464–9469.
- [22] H.Y.F. Sim, J.R.T. Chen, C.S.L. Koh, H.K. Lee, X. Han, G.C. Phan-Quang, J.Y. Pang, C.L. Lay, S. Pedireddy, I.Y. Phang, E.K.L. Yeow, X.Y. Ling, ZIF-Induced d-band modification in a bimetallic nanocatalyst: achieving Over 44% efficiency in the ambient nitrogen reduction reaction, *Angew. Chem. Int. Ed.* 59 (2020) 16997–17003.
- [23] X. Yu, P. Han, Z. Wei, L. Huang, Z. Gu, S. Peng, J. Ma, G. Zheng, Boron-doped graphene for electrocatalytic N₂ reduction, *Joule* 2 (2018) 1610–1622.
- [24] C. Liu, Q. Li, C. Wu, J. Zhang, Y. Jin, D.R. MacFarlane, C. Sun, Single-boron catalysts for nitrogen reduction reaction, *J. Am. Chem. Soc.* 141 (2019) 2884–2888.
- [25] C. Lv, C. Yan, G. Chen, Y. Ding, J. Sun, Y. Zhou, G. Yu, An amorphous noble-metal-free electrocatalyst that enables nitrogen fixation under ambient conditions, *Angew. Chem. Int. Ed.* 57 (2018) 6073–6076.
- [26] C. Wang, L.-L. Gu, S.-Y. Qiu, J. Gao, Y.-C. Zhang, K.-X. Wang, J.-J. Zou, P.-J. Zuo, X.-D. Zhu, Modulating CoFe2O4 nanocube with oxygen vacancy and carbon wrapper towards enhanced electrocatalytic nitrogen reduction to ammonia, *Appl. Catal. B Environ.* 297 (2021), 120452.
- [27] Y. Ohki, M.D. Fryzuk, Dinitrogen activation by group 4 metal complexes, *Angew. Chem. Int. Ed.* 46 (2007) 3180–3183.
- [28] I. Coric, B.Q. Mercado, E. Bill, D.J. Vinyard, P.L. Holland, Binding of dinitrogen to an iron-sulfur-carbon site, *Nature* 526 (2015) 96–99.
- [29] W.P. Utomo, M.K.H. Leung, Z. Yin, H. Wu, Y.H. Ng, Advancement of bismuth-based materials for electrocatalytic and photo(electro)catalytic ammonia synthesis, *Adv. Funct. Mater.* 32 (2021), 2106713.
- [30] M. Arif, G. Yasin, L. Luo, W. Ye, M.A. Mushtaq, X. Fang, X. Xiang, S. Ji, D. Yan, Hierarchical hollow nanotubes of NiFeV-layered double hydroxides@CoVP heterostructures towards efficient, pH-universal electrocatalytic nitrogen reduction reaction to ammonia, *Appl. Catal. B Environ.* 265 (2020), 118559.
- [31] P. Liu, K. Shi, W. Chen, R. Gao, Z.L. Liu, H. Hao, Y. Wang, Enhanced electrocatalytic nitrogen reduction reaction performance by interfacial engineering of MOF-based sulfides FeNi₂S₄/NiS heterointerface, *Appl. Catal. B Environ.* 287 (2021), 119956.
- [32] Y. Guo, Z. Yao, B.J.J. Timmer, X. Sheng, L. Fan, Y. Li, F. Zhang, L. Sun, Boosting nitrogen reduction reaction by bio-inspired FeMoS containing hybrid electrocatalyst over a wide pH range, *Nano Energy* 62 (2019) 282–288.
- [33] G. Qing, R. Ghazfar, S.T. Jackowski, F. Habibzadeh, M.M. Ashtiani, C.P. Chen, M. R. Smith 3rd, T.W. Hamann, Recent advances and challenges of electrocatalytic N₂ reduction to ammonia, *Chem. Rev.* 120 (2020) 5437–5516.
- [34] X. Wang, M. Luo, J. Lan, M. Peng, Y. Tan, Nanoporous intermetallic Pd₃Bi for efficient electrochemical nitrogen reduction, *Adv. Mater.* 33 (2021), e2007733.
- [35] J. Wang, B. Huang, Y. Ji, M. Sun, T. Wu, R. Yin, X. Zhu, Y. Li, Q. Shao, X. Huang, A general strategy to glassy M-Te (M=Ru, Rh, Ir) Porous Nanorods for Efficient Electrochemical N₂ Fixation, *Adv. Mater.* 32 (2020), e1907112.
- [36] M.M. Shi, D. Bao, B.R. Wu, Y.H. Li, Y.F. Zhang, J.M. Yan, Q. Jiang, Au sub-nanoclusters on TiO₂ toward highly efficient and selective electrocatalyst for N₂ conversion to NH₃ at ambient conditions, *Adv. Mater.* 29 (2017), 1606550.
- [37] J. Liang, P. Liu, Q. Li, T. Li, L. Yue, Y. Luo, Q. Liu, N. Li, B. Tang, A.A. Alshehri, I. Shakir, P.O. Agboola, C. Sun, X. Sun, Amorphous boron carbide on titanium dioxide nanobelts arrays for high-efficiency electrocatalytic NO reduction to NH₃, *Angew. Chem. Int. Ed.* 61 (2022), e202202087.
- [38] Y. Guo, J. Liu, Q. Yang, P. Khemthong, Z. Huang, Y. Zhao, Z. Chen, B. Dong, X. Fu, J. Luo, C. Zhi, Regulating nitrogenous adsorption and desorption on Pd clusters by

- the acetylene linkages of hydrogen substituted graphdiyne for efficient electrocatalytic ammonia synthesis, *Nano Energy* 86 (2021), 106099.
- [39] H. Shen, C. Choi, J. Masa, X. Li, J. Qiu, Y. Jung, Z. Sun, Electrochemical ammonia synthesis: mechanistic understanding and catalyst design, *Chem* 7 (2021) 1708–1754.
- [40] A. Biswas, S. Nandi, N. Kamboj, J. Pan, A. Bhowmik, R.S. Dey, Alteration of electronic band structure via a metal-semiconductor interfacial effect enables high faradaic efficiency for electrochemical nitrogen fixation, *ACS Nano* 15 (2021) 20364–20376.
- [41] Y. Fang, Y. Xue, L. Hui, H. Yu, Y. Li, Graphdiyne@janus magnetite for photocatalytic nitrogen fixation, *Angew. Chem. Int. Ed.* 60 (2021) 3170–3174.
- [42] P. Wang, W. Nong, Y. Li, H. Cui, C. Wang, Strengthening nitrogen affinity on CuAu@Cu core-shell nanoparticles with ultrathin Cu skin via strain engineering and ligand effect for boosting nitrogen reduction reaction, *Appl. Catal. B Environ.* 288 (2021), 119999.
- [43] D.K. Yesudoss, G. Lee, S. Shanmugam, Strong catalyst support interactions in defect-rich γ -Mo2N nanoparticles loaded 2D-h-BN hybrid for highly selective nitrogen reduction reaction, *Appl. Catal. B Environ.* 287 (2021), 119952.
- [44] Y. Zhang, Q. Zhang, D. Liu, Z. Wen, J. Yao, M. Shi, Y. Zhu, J.-M. Yan, Q. Jiang, High spin polarization ultrafine Rh nanoparticles on CNT for efficient electrochemical N₂ fixation to ammonia, *Appl. Catal. B Environ.* 298 (2021), 120592.
- [45] J. Zheng, Y. Lyu, M. Qiao, R. Wang, Y. Zhou, H. Li, C. Chen, Y. Li, H. Zhou, S. Jiang, S. Wang, Photoelectrochemical synthesis of ammonia on the aerophilic-hydrophilic heterostructure with 37.8% efficiency, *Chem* 5 (2019) 617–633.
- [46] Y. Yang, L. Zhang, Z. Hu, Y. Zheng, C. Tang, P. Chen, R. Wang, K. Qiu, J. Mao, T. Ling, S. Qiao, The crucial role of charge accumulation and spin polarization in activating carbon-based catalysts for electrocatalytic nitrogen reduction, *Angew. Chem. Int. Ed.* 59 (2020) 4525–4531.
- [47] X. Gao, Y. Shang, L. Liu, F. Fu, Chemisorption-enhanced photocatalytic nitrogen fixation via 2D ultrathin p-n heterojunction AgCl/δ-Bi₂O₃ nanosheets, *J. Catal.* 371 (2019) 71–80.
- [48] J. Peng, X. Chen, W. Ong, X. Zhao, N. Li, Surface and heterointerface engineering of 2D MXenes and their nanocomposites: insights into electro- and photocatalysis, *Chem* 5 (2019) 18–50.
- [49] Z. Dai, S.K. Yadavalli, M. Chen, A. Abbaspourtajani, Y. Qi, N.P. Padture, Interfacial toughening with self-assembled monolayers enhances perovskite solar cell reliability, *Science* 372 (2021).
- [50] Y. Zhao, R. Shi, X. Bian, C. Zhou, Y. Zhao, S. Zhang, F. Wu, G.I.N. Waterhouse, L. Z. Wu, C.H. Tung, T. Zhang, Ammonia detection methods in photocatalytic and electrocatalytic experiments: how to improve the reliability of NH₃ production rates? *Adv. Sci.* 6 (2019), 1802109.
- [51] L. Zhang, X. Ji, X. Ren, Y. Ma, X. Shi, Z. Tian, A.M. Asiri, L. Chen, B. Tang, X. Sun, Electrochemical ammonia synthesis via nitrogen reduction reaction on a MOS2 catalyst: theoretical and experimental studies, *Adv. Mater.* 30 (2018), e1800191.
- [52] S. Grimme, J. Antony, S. Ehrlich, H. Krieg, A consistent and accurate ab initio parametrization of density functional dispersion correction (DFT-D) for the 94 elements H-Pu, *J. Chem. Phys.* 132 (2010), 154104.
- [53] Z. Lin, Y. Huang, X. Duan, Van der Waals thin-film electronics, *Nat. Electron.* 2 (2019) 378–388.
- [54] C. Liu, G. Zhang, L. Yu, J. Qu, H. Liu, Oxygen doping to optimize atomic hydrogen binding energy on NiCoP for highly efficient hydrogen evolution, *Small* 14 (2018), e1800421.
- [55] Y. Fang, Y. Xue, Y. Li, H. Yu, L. Hui, Y. Liu, C. Xing, C. Zhang, D. Zhang, Z. Wang, X. Chen, Y. Gao, B. Huang, Y. Li, Graphdiyne interface engineering: highly active and selective ammonia synthesis, *Angew. Chem. Int. Ed.* 59 (2020) 13021–13027.
- [56] K. Chu, Y.P. Liu, Y.B. Li, Y.L. Guo, Y. Tian, Two-dimensional (2D)/2D interface engineering of a MoS₂/C₃N₄ heterostructure for promoted electrocatalytic nitrogen fixation, *ACS Appl. Mater. Interfaces* 12 (2020) 7081–7090.
- [57] H. Cheng, L.X. Ding, G.F. Chen, L. Zhang, J. Xue, H. Wang, Molybdenum carbide nanodots enable efficient electrocatalytic nitrogen fixation under ambient conditions, *Adv. Mater.* 30 (2018), e1803694.
- [58] W. Ye, M. Arif, X. Fang, M.A. Mushtaq, X. Chen, D. Yan, Efficient photoelectrochemical route for the ambient reduction of N₂ to NH₃ based on nanojunctions assembled from MoS₂ nanosheets and TiO₂, *ACS Appl. Mater. Interfaces* 11 (2019) 28809–28817.
- [59] D. Kong, H. Wang, Z. Lu, Y. Cui, CoSe₂ nanoparticles grown on carbon fiber paper: an efficient and stable electrocatalyst for hydrogen evolution reaction, *J. Am. Chem. Soc.* 136 (2014) 4897–4900.
- [60] H. Chen, J. Liang, K. Dong, L. Yue, T. Li, Y. Luo, Z. Feng, N. Li, M.S. Hamdy, A. A. Alshehri, Y. Wang, X. Sun, Q. Liu, Ambient electrochemical N₂-to-NH₃ conversion catalyzed by TiO₂ decorated Juncus effusus-derived carbon microtubes, *Inorg. Chem. Front.* 9 (2022) 1514–1519.
- [61] M.A. Mushtaq, M. Arif, X. Fang, G. Yasin, W. Ye, M. Basharat, B. Zhou, S. Yang, S. Ji, D. Yan, Photoelectrochemical reduction of N₂ to NH₃ under ambient conditions through hierarchical MoSe₂@g-C₃N₄ heterojunctions, *J. Mater. Chem. A* 9 (2021) 2742–2753.
- [62] J. Zheng, Y. Lyu, M. Qiao, J.P. Veder, R.D. Marco, J. Bradley, R. Wang, Y. Li, A. Huang, S.P. Jiang, S. Wang, Tuning the electron localization of gold enables the control of nitrogen-to-ammonia fixation, *Angew. Chem. Int. Ed.* 58 (2019) 18604–18609.
- [63] Y. Liu, L. Tang, J. Dai, J. Yu, B. Ding, Promoted electrocatalytic nitrogen fixation in Fe-Ni layered double hydroxide arrays coupled to carbon nanofibers: the role of phosphorus doping, *Angew. Chem. Int. Ed.* 59 (2020) 13623–13627.
- [64] Y. Yang, S. Wang, H. Wen, T. Ye, J. Chen, C.P. Li, M. Du, Nanoporous gold embedded ZIF composite for enhanced Electrochemical nitrogen fixation, *Angew. Chem. Int. Ed.* 58 (2019) 15362–15366.
- [65] Y. Yao, S. Zhu, H. Wang, H. Li, M. Shao, A spectroscopic study on the nitrogen electrochemical reduction reaction on gold and platinum surfaces, *J. Am. Chem. Soc.* 140 (2018) 1496–1501.